Machine learning aided design of smart, self-sensing fiber-reinforced plastics

Hyung Doh Roh [a,+], Dahun Lee [b,+], In Yong Lee [b], Young-Bin Park [b,*]

[a] Carbon Composites Department, Composites Research Division, Korea Institute of Materials Science (KIMS), Changwon, Gyeongnam 51508, South Korea
[b] Department of Mechanical Engineering, Ulsan National Institute of Science and Technology, UNIST-gil 50, Ulju-gun, Ulsan 44919, South Korea

ARTICLE INFO

ABSTRACT

Numerous techniques have been developed for the non-destructive evaluation (NDE) of impact damage in fiber reinforced plastics (FRPs), following the increasing demands for their safety and maintenance. Considering the large-scale detection and the vast amount of data involved, machine learning (ML) can be utilized in NDE for damage type analysis and impact damage localization. Furthermore, self-sensing using carbon fiber in FRPs is an emerging technique for NDE that can be combined with ML. In this study, ML was used to design smart FRPs by selecting the fiber type and electrode distance considering the cost and electromechanical sensitivity. Further-more, a novel algorithm for structural health self-sensing was suggested using an artificial neural network. The developed ML algorithms are advantageous since they do not require a theoretical model when all the factors and the variables of FRPs, such as the maximum absorbed impact energy, maximum impact force, initial electrical resistance, number of electrodes, fiber types, and electrode distance, are to be considered. The algorithm was trained using given input data and the target, and the output could be successfully obtained when new input data were provided. Therefore, the proposed ML algorithms hold great potential and applicability to FRP design and for NDE methods.

1. Introduction

Structural health monitoring (SHM) of fiber reinforced plastics (FRPs) has been analyzed in several studies for both the safety [1-3] and the maintenance cost [4-6] owing to the increase in the structural scale of the FRPs. There has been a particularly high demand for non-destructive evaluation (NDE), because internal failure such as matrix cracking and delamination can be observed without structural decomposition. Furthermore, condition-based NDE techniques such as FBG sensing [7, 8], strain gage sensing [9], and PZT sensing [10] are preferred over schedule-based inspection because they allow for the real-time monitoring of large-scale structures. In addition, self-sensing of FRP has been widely investigated based on the electrical resistance of conductive fibers [11-15].

FRPs are composed of various types of fibers such as carbon, aramid, and hybrid fibers. The hybrid fibers themselves are made of different types of fibers. Carbon fiber has superior mechanical properties in terms of the static load such as elastic modulus and strength to weight ratio [16-18]. Aramid fiber has superior properties under dynamic loading

such as impact with a comparable density [19, 20]. These two types of fibers, that is, the carbon and aramid fibers, can be fused together to form the carbon-aramid hybrid fiber, to combine the advantages of both the fibers [21, 22]. Therefore, the complexity of the carbon–aramid hybrid fiber increases due to the numerous characteristics of the two different fibers, which are mixed.

Machine learning (ML) is widely applied in various fields, as it can efficiently process enormous amounts of data [23]. ML enables decision-making based on training using vast amounts of inputs without the need for theoretical modeling. Furthermore, the performance of ML can be improved by tuning the training parameters, especially when an artificial neural network (ANN) is used. ANNs can be trained by using several sets of input data and the corresponding target, and the output can be generated without any theoretical intervention [24, 25]. For example, O. R. Aboudeh et al. [26] investigated ANN to design reinforced concrete bonded with FRP sheets. H. Naderpour and S. A. Alavi [27] also used ANN to analyze the shear contribution of FRP in reinforced concrete beams. The main novelty of their research is the simplicity of using ANN without separate modeling. ANN extracted the
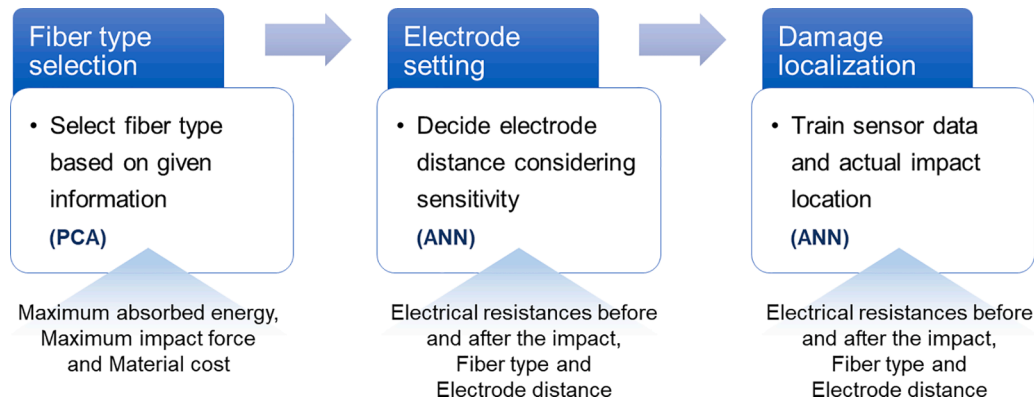
Fig. 1. Flow chart representing the methodologies applied in this study.

required output based on the training, which correlates the input and target data, and considered the parameters without the use of theoretical models. Therefore, machine learning is often utilized by SHM to enhance the capabilities of the monitoring systems.

In this paper, an ML aided real-time NDE and a FRP design using principal component analysis (PCA) and ANN are proposed to handle the uncountable variables of carbon–aramid hybrid fibers, as shown in Fig. 1. The fiber type and distance between the electrodes are considered in the design of self-sensing FRP, to provide an optimal material cost and sensing performance, respectively. Therefore, PCA is utilized to distinguish which given information is effective for selecting the appropriate fiber. PCA is used to highlight the distinctive features of unsorted information [28, 29]. It also identifies discriminative variables and classifies the information. Essentially, the input variables of the given data are re-identified by PCA and are classified using the determined variables.

Additionally, ANN was utilized to set the electromechanical sensitivity through training, based on the accumulated data. Damage localization is used in the ANN to localize the damaged locations in the coordinates based on the training. Various studies have verified the engineering approaches by comparing theoretical analysis and ANN outputs [30-32]. The ANN algorithm can easily draw the required output by using iterated weights and bias for correlating the input and target during training. Therefore, no additional modeling and algorithm for FRP design and NDE was required, but only accumulated data sets for training. The simplicity and precision of both composite design and NDE were comparatively investigated using conventional methods in this study. In particular, conventional damage localization using multiple sets of electrical resistance changes were analyzed as a control strategy.

2. Experimental and machine learning methodologies

2.1. Materials

The fiber used in this study was the 3K plain woven carbon fiber (Mitsubishi, Japan), and it was purchased from Jet Korea Corp. (Changwon, Korea). This fiber had a yarn type of T300SC, weight of 195 g/m^2, and thickness of 0.2 mm. Plain-woven carbon–aramid hybrid fibers supplied from JMC Corp. (Gyeongju, Korea) had carbon fibers in warp or weft, and the aramid fiber had a thickness of 0.25 mm. The plain-woven aramid fiber with a density of 165 g/m^2 and thickness of 0.25 mm and was purchased from Keun Young Industry (Seoul, Korea).

Polymer matrix used was vinylester, and its composition was 55 % epoxy acrylate and 45 % styrene (RF-1001MV, CCP Composites, Korea). The corresponding curing agent was methyl ethyl ketone peroxide (Arkema, France) crosslinker, and the mixing ratio of was 1.0 wt.% of the vinylester. Both the matrix and the curing agent were supplied from Jet Korea Corp. (Changwon, Korea). Electrode was installed using a 30 AWG copper wire and the silver paste (P-100, Elcoat, USA) to minimize contact resistance between the carbon fiber and the wire.

2.2. FRP manufacturing

All the FRPs were manufactured by vacuum assisted resin transfer molding. Before vacuum bagging, copper wires were embedded into electrically conductive carbon fibers to measure the electrical resistance. The specification of the copper wire used is 30 AWG: it has a diameter of 0.255 mm and an electrical resistance of 0.339 Ohm/m. The copper wire was embedded into the carbon fiber bundle to measure the changes in the electrical resistance. The contact length between the copper wire and the carbon fiber at the point of contact was more than 4 mm in order to secure the electrical contact and also minimize the electrical noise. Silver paste was applied at the conjunction, and it was dried for 2 minutes using a heating gun. The fibers containing the embedded
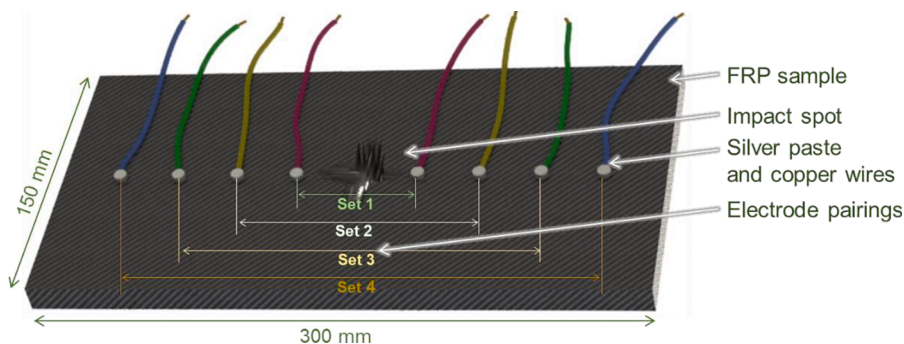

Fig. 2. Schematic of a FRP sample for electrode distance analysis.

Fig. 3. Schematic of a square FRP sample for damage localization.

Fig. 4. Flow chart of selecting fiber type using PCA.

electrodes were placed on the top plies. The peel ply was laid on these fibers, and the resin flow medium was laid on the top. The vacuum bag was used to seal the fibers with the help of sealant tape. The resin was infused into the vacuum bag through the pressure difference between the atmosphere and the vacuum inside the bag. The curing time was 24 hours at room temperature.

FRP samples for electrode distance analysis was manufactured as described in Fig. 2. Fiber stacking configurations for these samples consisted of six plies of either carbon fiber or carbon–aramid hybrid fiber, yielding carbon fiber reinforced plastic (CFRPs) and carbon-–aramid hybrid fiber reinforced plastics (HFRPs). The distances between electrode sets (such as set 1-5 in Fig. 2) were 20, 50, 100, 150, and 200 mm.

The samples for damage localization were made in a 150-mm-square with six plies of either carbon fiber or carbon–aramid hybrid fiber, as depicted in Fig. 3, and four electrodes. To obtain variety in sample thickness, CFRPs consisting of 12 plies of carbon fiber were additionally manufactured with the same electrode setting. The distance between adjacent electrodes was optimized to 60 mm.

2.3. Electromechanical characterization

Drop weight impact testing was performed using a drop weight impact testing tower (CEAST 9350, USA). A standard weight tup holder (#7520.021, CEAST, USA) was used in the drop weight impact testing tower. A hemispherical striker, with a diameter of 12.7 mm which obeys ASTM D3763, D7192, and D5628, was used in conjunction with the tup holder. The input impact energy was 50 J to allow all the FRP samples to penetrate. The clamping force applied to the samples was 40 N with circular clamps whose inner diameter was 40 mm. Figs. 2 and 3 depict the locations of the impact damages, i.e., at the center of the sample for the electrode distance effect and at the center of Channel 1 for the damage localization, respectively. Electrical resistances of the FRP samples were measured based on the 2-probe method using a multi-meter (Fluke 189, USA).

The probes of the multimeter were connected to the electrodes embedded in the FRP samples. The analysis of the electrode distance determines the electrical resistance of the electrode pairs. Four electrode pairs, in which the puncture was located at the center, were used to determine the change in the electrical resistance before and after the impact test, as shown in Fig. 2.

Four different pairs were analyzed for the damage localization, which are represented as Channel 1 ~ 4 in Fig. 3. Similar to the analysis for the electrode distance, the electrical resistance changes were monitored before and after the drop weight impact test.

For repeatability, all the FRP samples had seven specimens each, and the mechanical impact properties of CFRPs and HFRPs were investigated using mean values and their standard deviations.

Table 1
Theoretical models and parameters applied to FRPs.

Theoretical models	Effects applied to	Selection by PCA
Fiber type (Carbon fiber, aramid fiber, glass fiber, …)	Cost and mechanical behavior	Meet customers' requirements (variables) based on data clustering without theoretical models
Rule of mixture (Physical properties in terms of fiber volume fraction)	Physical properties in terms of energy, deformation, and load	
Fiber volume fraction (Volume fraction of fiber among the FRP)	Material cost, thickness, and physical properties	
Laminate plate theory (Mechanical properties of tensile, shear, and bending)	Quasi-static mechanical properties	

2.4. PCA for fiber type selection

PCA allows for the analysis of discriminative features for clustering the inputs and then re-enumerating these inputs based on the analyzed clusters. Hence, PCA can aid in designing self-sensing FRPs, in which several variables such as the fiber type, initial resistance, maximum absorbed energy, maximum impact force, and material cost, are involved. In PCA, orthogonal linear transformation of data is performed to form a new coordinate having the highest variance, via scalar projection. The transformation re-enumerates the inputs based on the identified clusters.

Representative mathematical equation of PCA vector $t_{k(i)}$ Image deleted. Please check.Image deleted. Please check.Image deleted. Please check.Image deleted. Please check.Image deleted. Please check.is as follows:

$$t_{k(i)} = x_{(i)} \cdot w_k \tag{1}$$

where $x_{(i)}$ is a row vector of n by p matrix, w_k is a weight of coefficient, which is $(w_1, …, w_l)_{(k)}$, $i=1,…n$, and $k=1,…l$. In addition, to maximize variance, the first weight vector w_1 should be

$$w_k = \underset{\|w\|=1}{\operatorname{argmax}}\left\{\sum_i t_{1(i)}^2\right\}(w_1, …, w_l)_{(k)} \tag{2}$$

Furthermore, the k th component can be calculated as follows:

$$\widehat{X_k} = X - \sum_{s=1}^{k-1} X\, w_{(s)} w_{(s)}^T \tag{3}$$

In this study, the accumulated data were sorted by the fiber type. Therefore, based on the given requirements, the fiber type can be determined by identifying the clusters in which all the requirements are
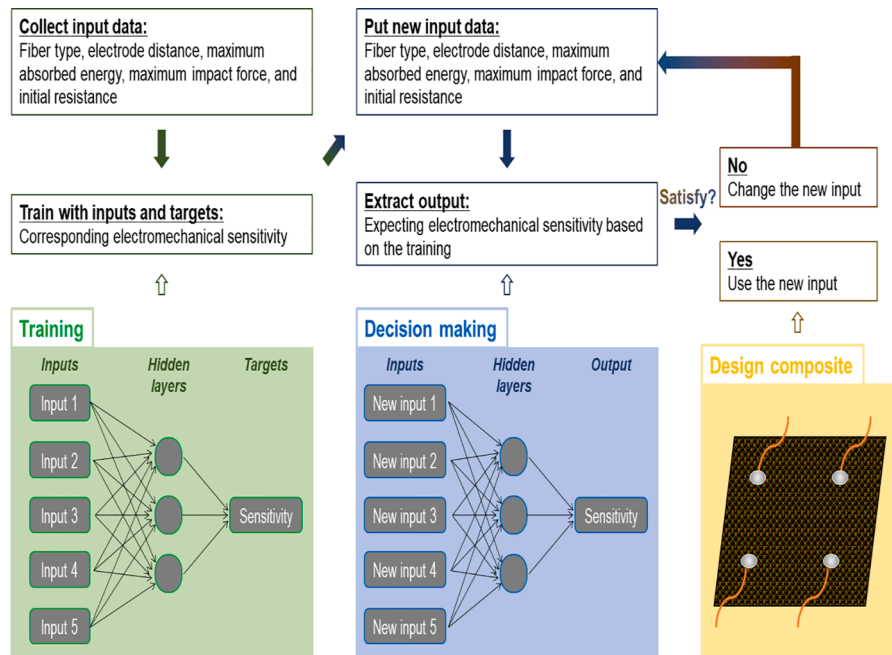
Fig. 5. Flow chart of electromechanical sensitivity using ANN.

met, as presented in Fig. 4. Particularly, PCA categorizes several data elements corresponding to their distinguishable parameters. Therefore, the error analysis for the PCA was omitted in this study. MATLAB, which is a commercialized software, was used for PCA. Ultimately, PCA is applied to the fiber selection to simplify various factors, parameters, and theoretical models. The traditional models used as examples for the fiber selection are listed in Table 1.

2.5. ANN for electrode distance analysis

ANN analyzes the inputs and the correlated targets using hidden layers, and this process is known as training. A trained ANN is therefore capable of determining the outputs even when the input data given is not known to the ANN. In training and decision making, no theoretical intervention is required. Therefore, ANN can be utilized to set the electromechanical sensitivity of self-sensing FRPs, because the sensitivity can be influenced by as many parameters as respective modeling or predicting is inefficient and laborious.

The training algorithm of ANN consists of input data and the cost function, which is dependent on the task and any a priori assumptions. For example, if there is a model as shown below,

$$f(x) = a \tag{4}$$

where a is a constant and the cost C is

$$C = E\left[(x - f(x))^2\right], \tag{5}$$

then the key function of ANN is to minimize the cost and let the value of a be equal to the mean of the data. Using these principles, electromechanical sensitivity can be estimated as an output considering several inputs. Otherwise, numerous electromechanical parameters should be considered, such as the electrical properties of fibers, electrical contact between adjacent fibers, orthotropic behavior of FRPs, electrode location, and distance between electrodes.

The overall procedure for determining the electromechanical sensitivity and other variables is shown in Fig. 5 as a closed loop; this loop remains closed until the required sensitivity can be satisfied. The ANN can be trained using several inputs and targets, and the new output can be extracted from the new inputs with the trained ANN. The training

function used was trainlm, which applied the Levenberg–Marquardt algorithm. Levenberg–Marquardt approaches second-order training speed without computing the Hessian matrix, which is

$$H = J^T J \tag{6}$$

and the gradient can be computed as

$$g = J^T e, \tag{7}$$

where J is the Jacobian matrix, which contains first derivatives of the network errors with respect to the weight and biases, and e is a vector of network errors. Eqns. (6) and (7) were utilized in the Levenberg–Marquardt algorithm as a Newton-like update, where μ is a scalar, as shown below:

$$x_{k+1} = x_k - \left[J^T J + \mu I\right]^{-1} J^T e \tag{8}$$

As the number of successful trainings increases, μ decreases. When μ becomes zero, Eqn. (8) becomes Newton's method. All of the procedures containing Eqns. (4)–(8) are included in the commercialized software, MATLAB.

The ANN is primarily trained on the basis of the pre-obtained datasets of the input and target; the precision of the ANN is validated based on the error between the estimated output and the empirical target data. The weights and bias of the ANN, which are its inherent network parameters, were acquired through the iterations of Eqns. (4)–(8) in the training stage, which is described as a hidden layer in Fig. 5. These equations are used for the iterations of weights and bias required to minimize the errors. These parameters remain unchanged after the training because the aforementioned error proves the validity of the ANN algorithm.

The input parameters are fiber type, electrode distance, maximum absorbed energy, maximum impact force, and initial resistance. The target or output is the corresponding electromechanical sensitivity. If the output does not meet the requirement, new inputs can be tuned and inserted into the ANN for the repetitive iteration of the procedure with the fixed parameters through the training.
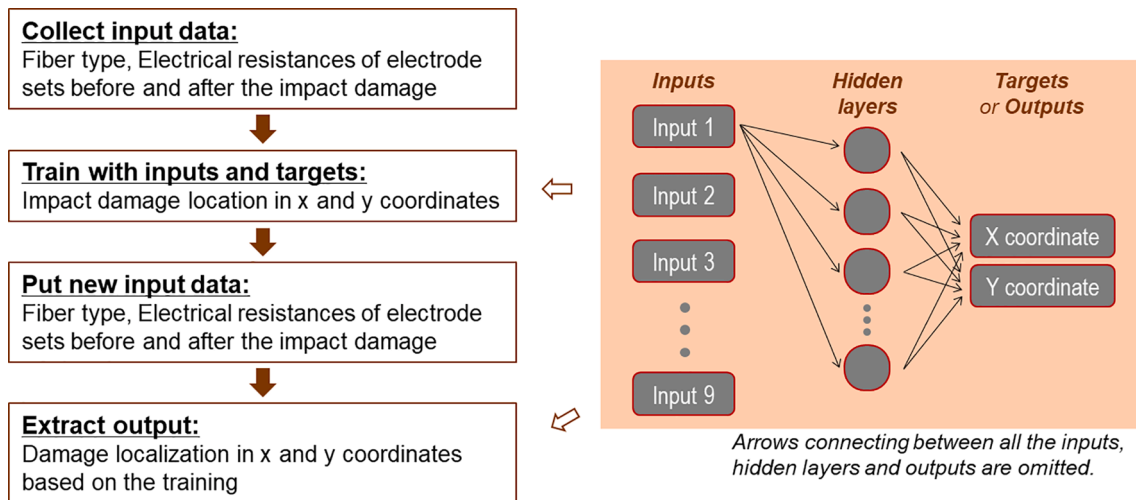
Fig. 6. Algorithm for damage localization using ANN.

Table 2
Impact mechanical properties of CFRPs and HFRPs in mean values and their standard deviations in brackets.

Samples	Maximum absorbed impact energy [J]	Maximum impact force [N]	Sample thickness [mm]
6-Ply-CFRP	9.40 (1.39)	2167 (507)	1.37 (0.03)
6-Ply-HFRP	8.43 (0.20)	1986 (323)	1.20 (0.02)
12-Ply-CFRP	29.69 (0.05)	7776 (242)	2.41 (0.02)

2.6. ANN for impact damage localization

The ANN algorithm can be built using correlating inputs and target, and the output can be extracted with respect based on the newly collected inputs in MATLAB. Similarly, non-destructive damage localizing algorithm can be realized with the ANN with several training sets of damage localization. As shown in Fig. 6, ANN can be trained by several inputs and targets based on Eqns. (4) and (5). The inputs given are the fiber type, and the electrical resistances of the electrode sets before and after the impact. The targets are the actual locations of impact damage in the x and y coordinates. The trained ANN localizes the impact location in terms of the coordinates with the new input data. Similar to the ANN that was used for determining the sensitivity, the damage localizing ANN can omit modeling and decision-making
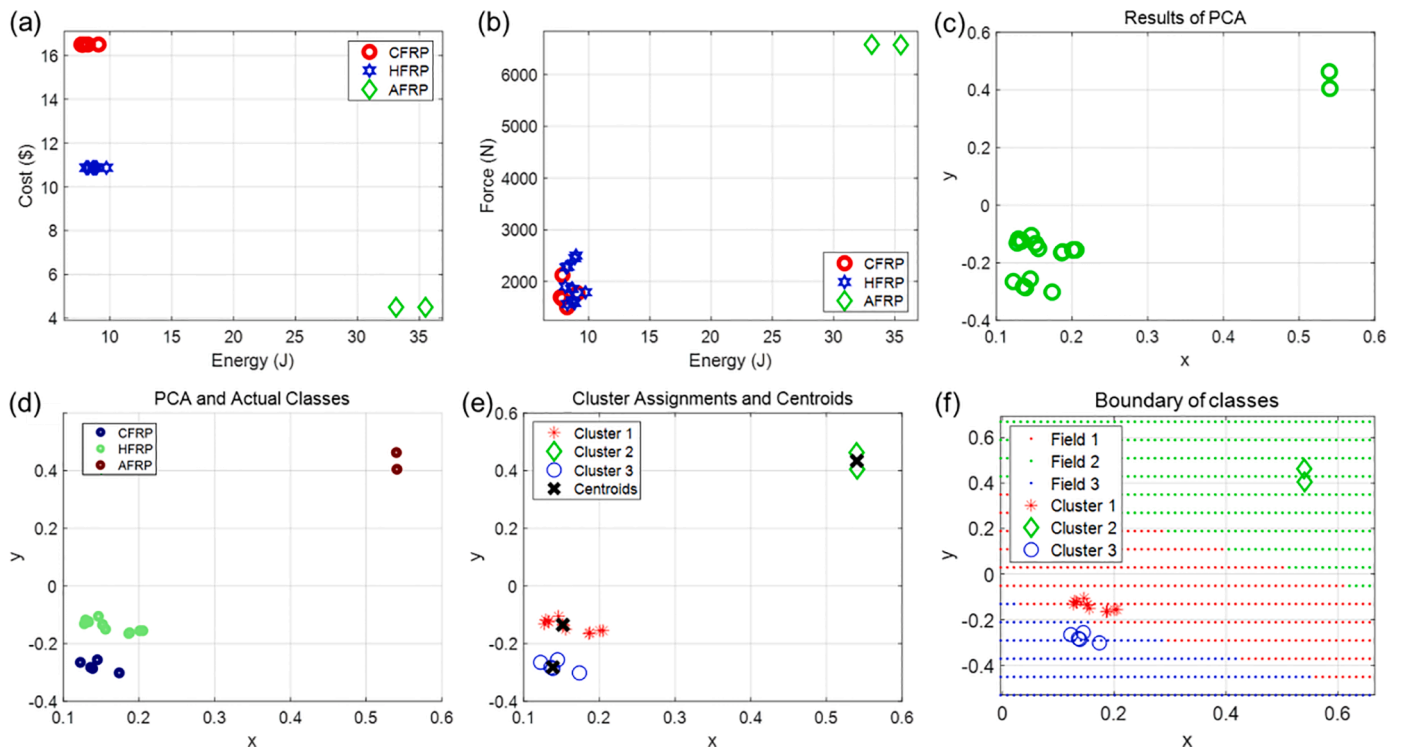
Fig. 7. Plots of (a) cost-energy, (b) force-energy, and (c) PCA results, (d) identifying PCA results based on given input data, (e) clustering PCA results, and (f) boundary of clustering boundaries.
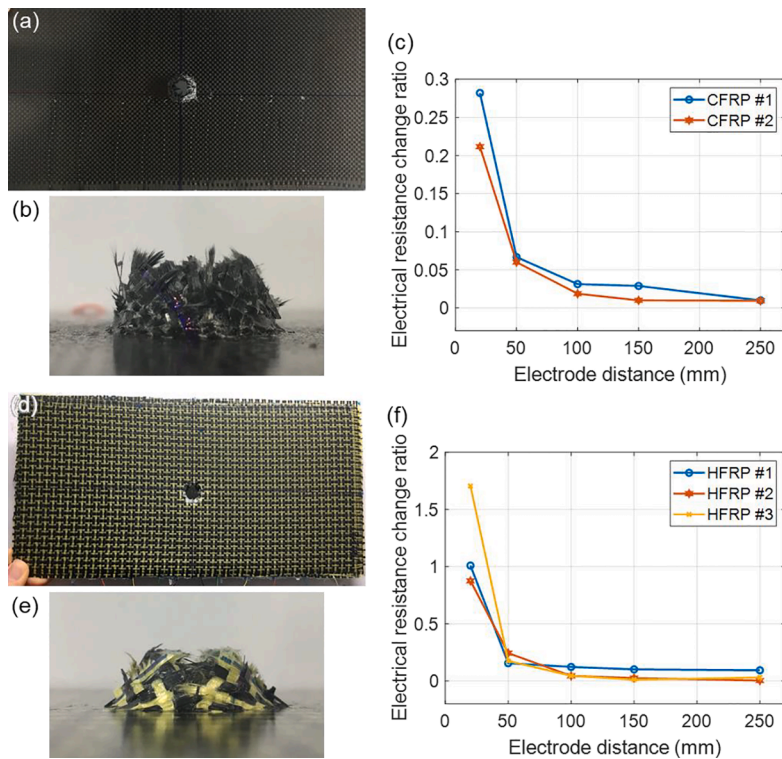
Fig. 8. Photos of the penetrated 6-ply-CFRP sample in (a) top view and (b) side view of the puncture. (c) Electrical resistance change ratio of the CFRP after the impact in terms of electrode distance. Photos of the penetrated 6-ply-HFRP sample in (d) top view and (e) side view of the puncture. (f) Electrical resistance change ratio of the HFRP after the impact in terms of electrode distance.

parameters of the respective FRP samples.

The control method used for impact damage localization was also developed using MATLAB. The geometries of the FRP samples, the locations of electrodes, and the mid-points of electrical channels were all set as 2D coordinates in x–y planes. In the MATLAB code, the mid-point of the channel, which showed the largest electrical resistance change ratio, was identified, and the resistance change ratio was multiplied. From that coordinate, the mid-points of other channels and each resistance change ratio were multiplied with x_{weight} and y_{weight} into the x and y coordinates, respectively. The weights x_{weight} and y_{weight} were optimized to produce the minimum localizing error.

3. Results and discussion

3.1. Fiber type selection

FRP involves several variables and parameters, which renders the designing of FRPs complicated. The impact mechanical properties of CFRPs and HFRPs are listed in Table 2. This table also contains the mean values of impact energy, impact force, and sample thickness, with their standard deviations written in brackets.

In the design process, fiber selection must consider users' needs; cost, maximum impact energy, and maximum impact force. The appropriate FRP fibers can be selected considering the cost and energy, as shown in Fig. 7(a); however, they do not sufficiently represent the data separability, as shown in Fig. 7(b), which illustrates the maximum impact force and the absorbed maximum impact energy of FRPs. Similarly, the identification of useful data is difficult as some parameters lack discernment, as shown Fig. 7(b). Therefore, PCA was performed, and the inputs introduced in section 2.4 were redistributed on the x-y plane, as shown in Fig. 7(c) and following Eqns. (1)–(3). The algorithm of PCA transforms either the axis or the data projection to maximize the separability, which attributes for the larger distance represented by the data in Fig. 7(c) between the clusters when compared to that of Fig. 7(b).

The actual classes of the FRPs are depicted in Fig. 7(d); these classes were re-enumerated in the x-y plane. Clustering results from the PCA with the centroids of the clusters are shown in Fig. 7(e). The clustering procedure is one of inherent algorithms of the PCA and can be used as a further process of data identification. As can be seen, clustering was successful as compared to that shown in Fig. 7(d). The boundaries of each cluster are represented in the x-y plane, as shown in Fig. 7(f). New input sets can be identified and enumerated in the x-y plane to classify the fields of the FRPs' requirements. Therefore, the requirements of the FRP can be analyzed using PCA to identify the associated clusters, and hence, appropriate fibers can be selected. Furthermore, the fibers are not limited to plain-woven fibers, as shown in Fig. 7, but contained as unidirectional, satin, and twill fibers, among others. Fiber selection should be considerably investigated to design appropriate FRPs in terms of the mechanical properties and manufacturing cost.

3.2. Electrode distance analysis

CFRPs and HFRPs showed fiber failure at the impact spots as shown in Fig. 8(a), (b), (d), and (e). Even though the input impact energy was large enough to penetrate the FRP samples, the fibers absorbed the energy so that the puncture sizes of the samples were similar to the diameter of the impact striker, which was ⌀12.7 mm. Compared to isotropic materials such as acrylic plate, the mechanical damage due to the impact was only limited to the struck area.

Electrical resistance change ratios of the CFRPs and HFRPs are shown in Fig. 8(c) and 8(f), respectively. Changes in the electrical network via electrically conductive carbon fiber due to punctures caused the electrical resistance increase; this is because the effective electrical network was detoured around the puncture. This result concurs with those of other studies in that mechanical deformation and corresponding electrical property change can be utilized as structural health monitoring [33-36]. The electrical resistance is calculated by the length, resistivity, and the cross-sectional area of the lowest option as electrons choose the
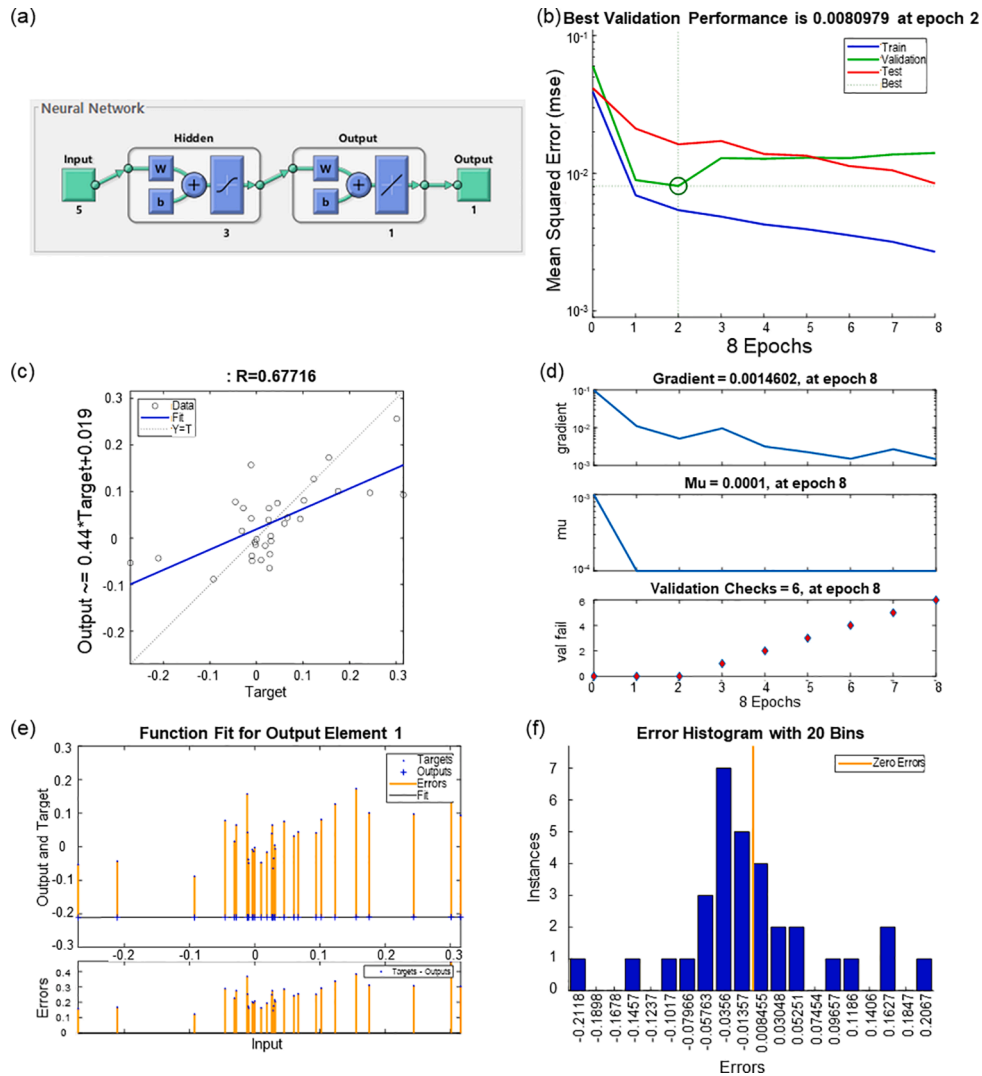
Fig. 9. Progress of ANN for electrode distance analysis minimizing the errors: (a) ANN structure, (b) MSE analysis, (c) Error analysis, (d) Output-target analysis (e) Error in terms of inputs, and (f) Error histogram

easiest path. The change in the resistance can be obtained by using the following equation:

$$\Delta R = \rho \, \frac{\Delta l}{A} \qquad (9)$$

where ΔR represents the change in the electrical resistance, ρ is the electrical resistivity of a material, Δl is change in length, and A represents the cross-sectional area. The detour increases the length ensuring the feasibility of electromechanical self-sensing.

Electromechanical sensitivity of a CFRP was smaller than that of a HFRP regardless of the electrode distance, because the CFRP secured more electrical networks than the HFRP after the impact. Essentially, the electrical detour in the CFRP was not as critical as the network change in the HFRP after the impact.

Additionally, the global deformation of a CFRP can also indicate the availability of electromechanical self-sensing [37]. The electrical resistances changed in different ways in various directions corresponding to the loading directions. Similar to classic laminate plate theory, the global elongation can be modelled by utilizing the gauge factor and electrical resistance. However, this study only addresses the impact puncture, which was relevant to the electrical detour.

Electrode pairings with distances of 20, 50, and 100 mm represented a distinctive resistance change ratio, but the change ratio decreased as

the distance between the electrodes increased as shown in Fig. 8(c) and 8 (f). Both the CFRPs and HFRPs showed slight changes in the electrical network when the distance between the electrodes was larger than 100 mm. The change ratio of the electrical resistance indicates the change in the electrical network. In other words, the larger electrode distance, the smaller was the change in the network.

Consider that the puncture diameter is 12.7 mm, the distance between electrodes is l, the width of the electrical network is w, and the thickness of the sample is t. Subsequently, the reduced volume ratio due to the puncture in the composite sample is as shown below:

$$\textit{Puncture area ratio} = \ 12.7^2 \pi \big/ 4 \ \times t \big/ (l \ w \ t) \qquad (10)$$

The width and the thickness are out of interest when we analyze the effect of electrode distance in one sample. Then, the decisive variable of the reduced mechanical volume and electrical network is l, the distance between electrodes. Therefore, the electrode distance should be thoroughly investigated and optimized considering its self-sensing sensitivity.

Seven specimens per sample showed similar behavior to those presented in Figs. 8(c) and 8(f), in order to ensure both the reproducibility and the performance of ANN [38]. Neither the deviation nor variation of anisotropic and heterogeneous FRP materials was effective for the electromechanical sensitivity in terms of the electrode distance. Even
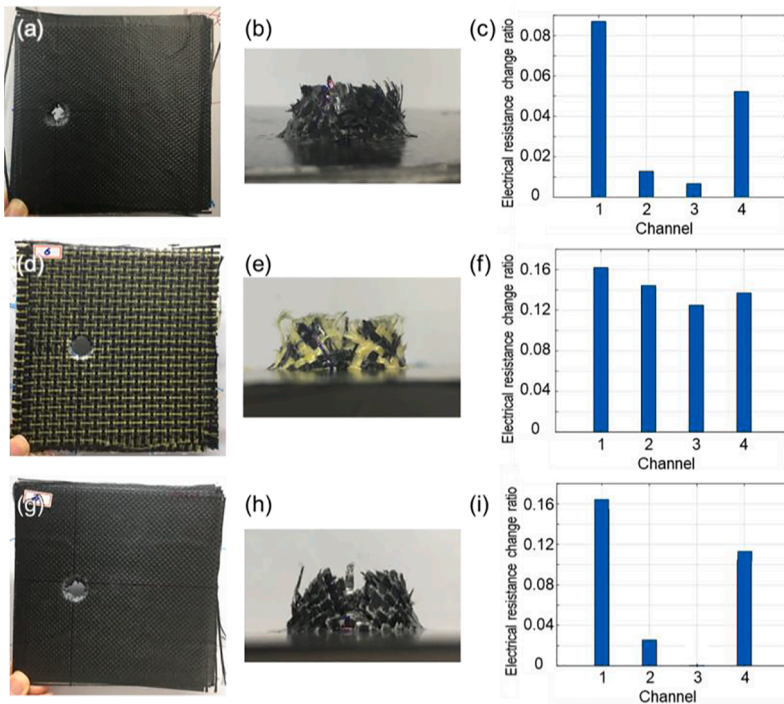
Fig. 10. Photos of the penetrated 6-ply-CFRP sample in (a) top view and (b) side view of the puncture. (c) Electrical resistance change ratio of the 6-ply-CFRP after the impact in terms of electrode distance. Photos of the penetrated 6-ply-HFRP sample in (d) top view and (e) side view of the puncture. (f) Electrical resistance change ratio of the 6-ply-HFRP after the impact in terms of electrode distance. Photos of the penetrated additional CFRP sample with 12 plies of carbon fibers in (g) the top view and (h) the side view of the puncture. (i) Electrical resistance change ratio of the 12-ply-CFRP after the impact in terms of electrode distance.

the mechanical changes, such as the shape of the impact punctures, were all similar among the various specimens.

This study was designed to analyze the electrical detour caused by impact punctures, and hence, the input impact energy was large enough for penetration. If the impact energy had been lesser than the amount required for the puncture, the damage size might be proportional to the input energy [39]. When the input energy was large enough for penetration, the absorbed impact energy of a material became saturated [40]. The changed magnitude of electrical resistance might be proportional to the crack size from the perspective of the electrical signal. Essentially, the change in the resistance might be proportional to the input impact energy [41, 42]. However, when the absorbed impact energy is saturated, both the crack size and the electrical resistance change also become saturated. Therefore, this study intentionally provided a large impact energy for the sample to be penetrated, following which, the changes in the electrical resistance were analyzed corresponding to the electrical detour along the puncture.

ANN described in Fig. 9(a) trained the correlation between the FRP information and the sensitivity, and its progress in minimizing the errors is shown in Fig. 9(b)-(f). The training data are marked in the graphs and the corresponding information can be acquired from the labels in the graph. The performance score of the ANN measured from the MATLAB software was 0.0080979. The performance score is a mean square error (MSE) calculated as shown below:

$$MSE = \frac{1}{n} \sum_{t=1}^{T} \left[\widehat{y}_t - y_t \right]^2 \tag{11}$$

where T is the number of predictions, t is time as an integer, $\widehat{y}_t$ is the predicted value, and y_t is a dependent variable. Notably, a lower score indicates a better training performance as the lower MSE was observed. The training was as successful as the comparable score acquired at epoch 2. Moreover, the error histogram obtained, as shown in Fig. 9(f), was reasonable in that it showed a normal distribution. The number of data elements used in this ANN was 32, and hence, 32 instances are represented in the error histogram, Fig. 9(f).

The expected sensitivity induced from the random input was 12.71 %, which was calculated by the trained ANN. The sensitivity was analyzed using the mean absolute percentage error (MAPE) as shown below:

$$MAPE = \frac{100}{T} \sum_{t=1}^{T} \frac{\widehat{y}_t - y_t}{y_t} \tag{12}$$

It presented a MAPE of 3.17% when compared to the empirical data. The process calculating the desired sensitivity contains the tuning of both the electromechanical sensitivity, which is the output, and the mechanical properties, which are the inputs. This algorithm can also be adapted to the nanomaterial reinforced composites which exhibit superior mechanical properties and electromechanical sensitivities [43, 44]. The dynamic-load-self-sensing of nanomaterial-composites using ANN can be developed in terms of both the mechanical reinforcement and material functionalization in a future study.

Using the developed ANN, the electromechanical sensitivity of the self-sensing aspect can be estimated, and it can be considered in composite design as represented in Fig. 5. In contrast, conventional studies obtained the sensitivity through empirical methods after the composite structures were completely manufactured [11-15]. Therefore, the proposed ANN model for a sensitivity analysis of the self-sensing composite can potentially save cost, time, and labor for composite manufacturing.

Furthermore, V. Kushvaha et al. [45-47] employed ANN for the analysis of impact properties. They successfully trained the ANN algorithms to estimate the stress intensity factors (SIFs) and fracture toughness of composites in terms of the shapes and contents of the nano-fillers. They also developed algorithms for the predictive modelling of the fracture behavior of silica-filled polymer composites providing SIFs and fracture toughness.

3.3. Impact damage localization

Impacted spots are observed, as shown in Fig. 10(a), (b), (d) (e), (g), and (h), similar to Fig. 8(a), (b), (d) and (e). The overall geometry of the FRP samples were irrelevant to the shape of the impacted area, and as such, the fibers that the impact striker hit were broken.

Electrical resistance change ratios of the 6-ply-CFRP and the 6-ply-HFRP of the four channels are shown in Fig. 10(c) and 10(f), respectively. The impacted area, which is channel 1, showed the largest
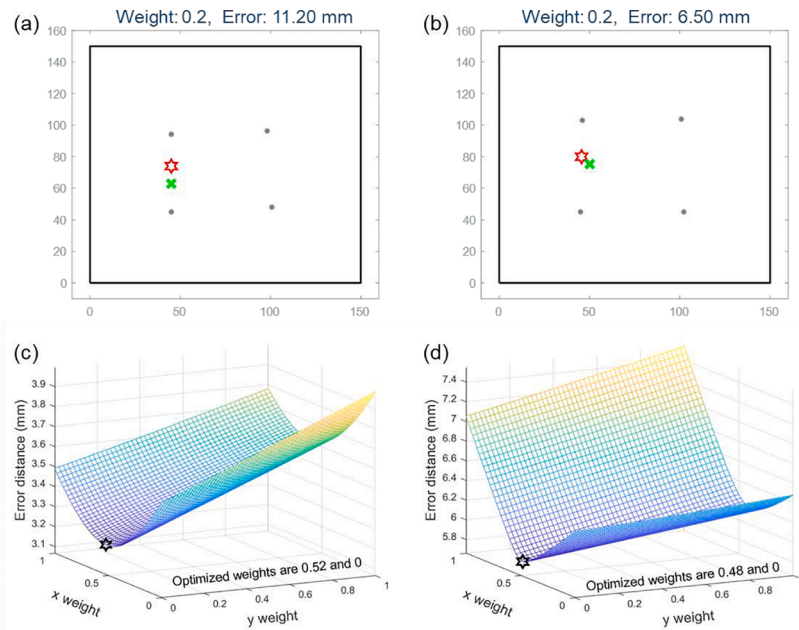
Fig. 11. Damage localization of (a) the CFRP and (b) the HFRP. Optimizing results for the weight factor of damage localization of (c) the CFRP and (d) the HFRP.

electrical resistance change. Electromechanical results of the12-ply-CFRP were similar to those of the 6-ply-CFRP as shown in Fig. 10(i). Neither the thickness nor the number of carbon fiber plies affected the electromechanical self-sensing mechanism. Even though all the channels of the HFRP showed an increase in the electrical resistance, it showed a larger electromechanical sensitivity at channel 1 compared to that of the CFRP. Likewise, damage localization can be performed by the four sections between the electrodes with different electromechanical sensitivities in terms of the fiber types.

Advanced conventional damage localizations of the CFRP and HFRP were performed as shown in Figs. 11(a) and 11(b), respectively. Damaged coordinates were calculated by a combination of multiple electrode sets instead of four larger and broader sections, which were introduced in Fig. 10. The channel that showed the largest electrical resistance was detected, and then other coordinates of the channels were multiplied with the resistance change ratio and weight. Essentially, the coordinate of the midpoint of the channel was multiplied by the change in the electrical resistance. Four different channels repeated the multiplication for the localization using the weight, and the summation of the multiplied values were divided by the number of channels. This process was performed in 2D using the x and y coordinates. In Figs. 11(a) and 11(b), x_{weight} and y_{weight} of the CFRP and HFRP were both 0.2, which was optimized by repetitive trials.

The optimization for the weights was investigated as shown in Figs. 11(c) and 11(d). The localizing errors of the FRPs were analyzed by controlling the weights. Although the optimized weights in this study were extracted as shown in Figs. 11(c) and 11(d), users should avoid a y_{weight} value of zero because it artificially limits the y-directional sensing.

To improve the sensing unit from the empirical data, ANN for impact damage localization was executed as shown in Fig. 12(a). The size of the hidden layer was modified to be the average of the inputs and outputs. The training score was 20.768 at epoch 2, as shown in Fig. 12(b). The training data are marked in the graphs, and the corresponding information can be acquired from the labels in the graph. MSE is also shown in Fig. 12(b) and was calculated as shown in Eqn. (11). The score was therefore higher than that acquired at section 3.2. As shown in Fig. 12(c), the error rate of the training was as small as the coefficient of determination was 0.9474. The error histogram represents 26 normally distributed instances, as shown in Fig. 12(f).

The output of the damage localization derived from the ANN, as shown in Fig. 12(a), is demonstrated in Fig. 13, by comparing the actual impact location and the estimated one. Both the CFRP and HFRP showed reliable damage localization results. While damage localization based on the empirical data analysis (as shown in Fig. 10) was limited to four wider sensing units, the ANN was able to extract the damage location in the x and y coordinates. Regardless of the electrical resistance variation, the trained ANN made a decision through the hidden layers. The underlying decision-making process is based on the similarity analysis between the trained sets and the new input, but not the analysis with electrical resistance changes before and after the impact as introduced in Fig. 10(c) and 10(f). The ANN was trained with multiple sets of input and target values. Subsequently, new inputs were analyzed with the trained ANN to acquire the output required by the users. In this study, the output includes the x and the y coordinates for the damage localization. In addition, the fiber type does not limit the sensing capability so self-sensing using electrical resistance and ANN is applicable to any carbon-material-based FRPs which holds electrical conductivity.

The errors of the expected localizations of a CFRP and an HFRP were 2.31 mm and 1.15 mm, respectively, compared to the actual location. These errors in distance scale are considered as types of MSE because the coordinates in the x and y directions were analyzed in Eqn. (11).

Compared to the conventional localization, whose minimum error was 6.50 mm, the self-sensing performance of the developed ANN was improved. Moreover, the ANN does not distinguish between fiber type or fiber stacking configuration because it correlates input and output numerically as introduced in Eqns. (4)–(8) with the minimum MSE following Eqn. (11). Therefore, impact damage localization with the ANN was successful with a higher sensing performance without any modeling than previous localization, which was introduced in Figs. 10 (c), 10(f), 11(a), and 11(b). Furthermore, self-sensing performance can be enhanced as more empirical data are accumulated [38].

4. Conclusion

We designed and analyzed smart self-sensing FRP using electrical resistance aided by ML methodologies such as the PCA and ANN. PCA was used to identify the discriminative features of FRPs to choose the appropriate materials. In addition, it helped classify the clusters in the given information. ANNs were utilized to set the electromechanical sensitivity and localize impact spots in x and y coordinates with
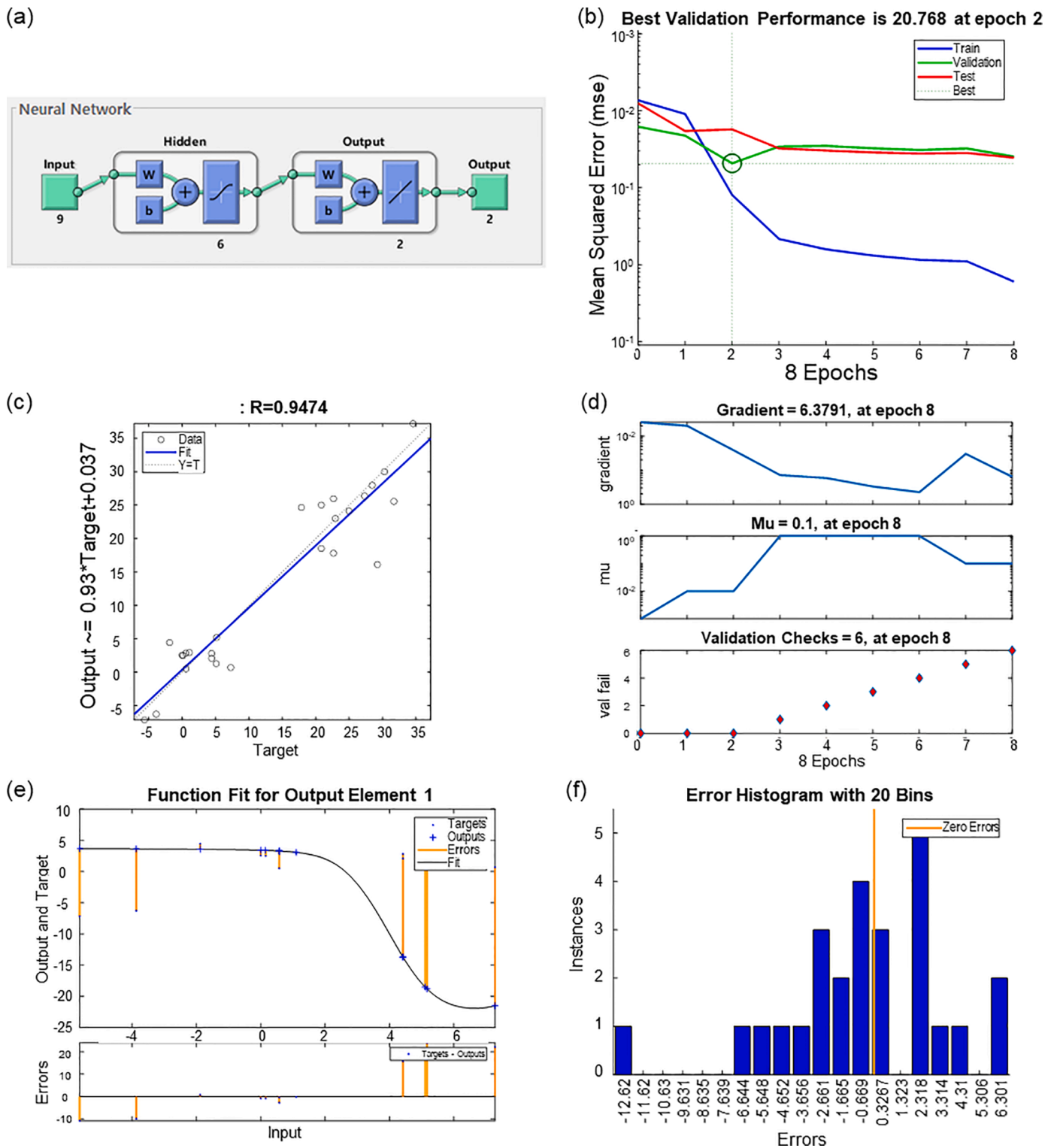
Fig. 12. Progress of ANN for impact damage localization minimizing the errors: (a) ANN structure, (b) MSE analysis, (c) Error analysis, (d) Output-target analysis (e) Error in terms of inputs, and (f) Error histogram

improved sensing performance. The use of ANNs can help avoid time-consuming and laborious empirical optimization.

Considering the numerous variables of an FRP, the ANNs could make accurate decisions in terms of sensitivity and localization. The primary advantage of the ANN-based algorithms developed in this study lies in that no electromechanical model was required for the smart FRPs. The trained algorithm could easily extract the output based on the given input. This shows the great potential of ML methodologies for NDE techniques that involve several variables. Specifically, the number of electrodes can be reduced to enhance the performance of large-scale FRPs in terms of accuracy and sensing performance.

The underlying novelty of this research is the ML aided designing to make a self-sensing CFRP. As future work, user-experience design or user-interface requirements can be analyzed to realize a smart factory
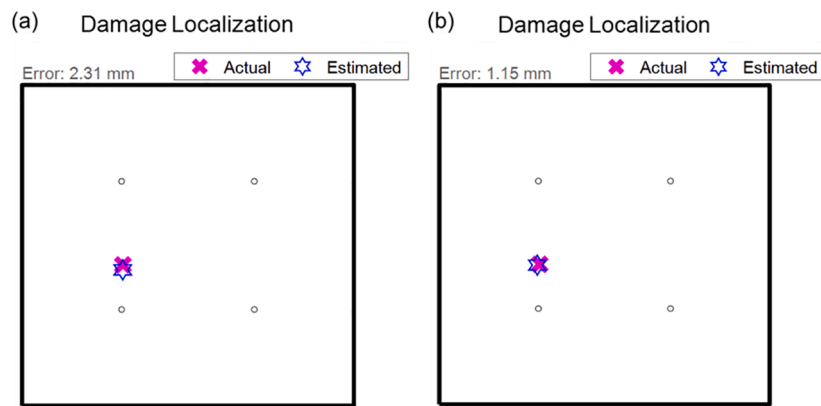
Fig. 13. Results of damage localization and error analysis of (a) a CFRP and (b) a HFRP.

producing customized and smart FRPs, in line with Industry 4.0.

Declaration of Competing Interest

The authors declare that they have no known competing financial interests or personal relationships that could have appeared to influence the work reported in this paper.

Acknowledgments

References

[1] G.C. Kahandawa, J. Epaarachchi, H. Wang, K. Lau, Use of FBG sensors for SHM in aerospace structures, Photonic Sensors 2 (3) (2012) 203–214.

[2] G.J. Gallo, E.T. Thostenson, Spatial damage detection in electrically anisotropic fiber-reinforced composites using carbon nanotube networks, Compos. Struct. 141 (2016) 14–23, https://doi.org/10.1016/j.compstruct.2015.07.082, https://doi.org/.

[3] M. Dziendzikowski, A. Kurnyta, K. Dragan, S. Klysz, A. Leski, In situ Barely Visible Impact Damage detection and localization for composite structures using surface mounted and embedded PZT transducers: A comparative study, Mech. Syst. Sig. Process. 78 (2016) 91–106, https://doi.org/10.1016/j.ymssp.2015.09.021, https://doi.org/.

[4] A. Philipp, G. Martin, K. Benjamin, Development of a small-scale and low-cost SHM system for thin-walled CFRP structures based on acoustic emission analysis and neural networks, in: Proc.SPIE, 2019, https://doi.org/10.1117/12.2518439.

[5] R. Soman, K. Majewska, M. Mieloszyk, P. Malinowski, W. Ostachowicz, Application of Kalman Filter based Neutral Axis tracking for damage detection in composites structures, Compos. Struct. 184 (2018) 66–77, https://doi.org/10.1016/j.compstruct.2017.09.092, https://doi.org/.

[6] C. Cherif, E. Haentzsche, R. Mueller, A. Nocke, M. Huebner, M.M.B. Hasan, 15 - Carbon fibre sensors embedded in glass fibre-based composites for windmill blades, in: V. Koncar (Ed.), Smart Textiles and their Applications, Woodhead Publishing, Oxford, 2016, pp. 329–352.

[7] K. Al Handawi, N. Vahdati, P. Rostron, L. Lawand, O. Shiryayev, Strain based FBG sensor for real-time corrosion rate monitoring in pre-stressed structures, Sens. Actuators B 236 (2016) 276–285, https://doi.org/10.1016/j.snb.2016.05.167, https://doi.org/.

[8] S. Mekid, A.M. Butt, K. Qureshi, Integrity assessment under various conditions of embedded fiber optics based multi-sensing materials, Opt. Fiber Technol. 36 (2017) 334–343, https://doi.org/10.1016/j.yofte.2017.05.010, https://doi.org/.

[9] B. Denkena, J. Kiesner, Strain gauge based sensing hydraulic fixtures, Mechatronics 34 (2016) 111–118, https://doi.org/10.1016/j.mechatronics.2015.05.008, https://doi.org/.

[10] M. Dziendzikowski, P. Niedbala, A. Kurnyta, K. Kowalczyk, K. Dragan, Structural Health Monitoring of a Composite Panel Based on PZT Sensors and a Transfer Impedance Framework, Sensors 18 (5) (2018) 1521.

[11] N. Kalashnyk, E. Faulques, J. Schjødt-Thomsen, L.R. Jensen, J.C.M. Rauhe, R. Pyrz, Monitoring self-sensing damage of multiple carbon fiber composites using piezoresistivity, Synth. Met. 224 (2017) 56–62, https://doi.org/10.1016/j.synthmet.2016.12.021, https://doi.org/.

[12] A. Todoroki, Y. Samejima, Y. Hirano, R. Matsuzaki, Piezoresistivity of unidirectional carbon/epoxy composites for multiaxial loading, Compos. Sci.

[13] Technol. 69 (11) (2009) 1841–1846, https://doi.org/10.1016/j.compscitech.2009.03.023, https://doi.org/.

[13] J.L. Abot, Y. Song, M.S. Vatsavaya, S. Medikonda, Z. Kier, C. Jayasinghe, N. Rooy, V.N. Shanov, M.J. Schulz, Delamination detection with carbon nanotube thread in self-sensing composite materials, Compos. Sci. Technol. 70 (7) (2010) 1113–1119, https://doi.org/10.1016/j.compscitech.2010.02.022, https://doi.org/.

[14] T. Yamane, A. Todoroki, Electric potential function of oblique current in laminated carbon fiber reinforced polymer composite beam, Compos. Struct. 148 (2016) 74–84, https://doi.org/10.1016/j.compstruct.2016.03.047, https://doi.org/.

[15] D. Wang, D.D.L. Chung, Through-thickness piezoresistivity in a carbon fiber polymer-matrix structural composite for electrical-resistance-based through-thickness strain sensing, Carbon 60 (2013) 129–138, https://doi.org/10.1016/j.carbon.2013.04.005, https://doi.org/.

[16] M. Sharma, S. Gao, E. Mäder, H. Sharma, L.Y. Wei, J. Bijwe, Carbon fiber surfaces and composite interphases, Compos. Sci. Technol. 102 (2014) 35–50, https://doi.org/10.1016/j.compscitech.2014.07.005, https://doi.org/.

[17] D.C. Davis, J.W. Wilkerson, J. Zhu, V.G. Hadjiev, A strategy for improving mechanical properties of a fiber reinforced epoxy composite using functionalized carbon nanotubes, Compos. Sci. Technol. 71 (8) (2011) 1089–1097, https://doi.org/10.1016/j.compscitech.2011.03.014, https://doi.org/.

[18] Z. Jia, T. Li, F.-p. Chiang, L. Wang, An experimental investigation of the temperature effect on the mechanics of carbon fiber reinforced polymer composites, Compos. Sci. Technol. 154 (2018) 53–63, https://doi.org/10.1016/j.compscitech.2017.11.015, https://doi.org/.

[19] J.G. Carrillo, R.A. Gamboa, E.A. Flores-Johnson, P.I. Gonzalez-Chi, Ballistic performance of thermoplastic composite laminates made from aramid woven fabric and polypropylene matrix, Polym. Test. 31 (4) (2012) 512–519, https://doi.org/10.1016/j.polymertesting.2012.02.010, https://doi.org/.

[20] G.V. Seretis, P.K. Kostazos, D.E. Manolakos, C.G. Provatidis, On the mechanical response of woven para-aramid protection fabrics, Compos. Part B Eng. 79 (2015) 67–73, https://doi.org/10.1016/j.compositesb.2015.04.025, https://doi.org/.

[21] J.H. Song, Pairing effect and tensile properties of laminated high-performance hybrid composites prepared using carbon/glass and carbon/aramid fibers, Compos. Part B Eng. 79 (2015) 61–66, https://doi.org/10.1016/j.compositesb.2015.04.015, https://doi.org/.

[22] Y. Zheng, Y. Sun, J. Li, L. Limin, L. Chen, J. Liu, S. Tian, Tensile response of carbon-aramid hybrid 3D braided composites, Mater. Des. 116 (2017) 246–252, https://doi.org/10.1016/j.matdes.2016.11.082, https://doi.org/.

[23] E.P. Xing, Q. Ho, W. Dai, J.K. Kim, J. Wei, S. Lee, X. Zheng, P. Xie, A. Kumar, Y. Yu, Petuum: A New Platform for Distributed Machine Learning on Big Data, IEEE Trans. Big Data 1 (2) (2015) 49–67, https://doi.org/10.1109/TBDATA.2015.2472014, https://doi.org/.

[24] E. Hodo, X. Bellekens, A. Hamilton, P. Dubouilh, E. Iorkyase, C. Tachtatzis, R. Atkinson, Threat analysis of IoT networks using artificial neural network intrusion detection system, in: 2016 International Symposium on Networks, Computers and Communications (ISNCC), 2016, pp. 1–6, https://doi.org/10.1109/ISNCC.2016.7746067, https://doi.org/.

[25] M. van Gerven, S. Bohte, Editorial: Artificial Neural Networks as Models of Neural Information Processing, Front. Comput. Neurosci. 11 (114) (2017), https://doi.org/10.3389/fncom.2017.00114 https://doi.org/.

[26] O.R. Abuodeh, J.A. Abdalla, R.A. Hawileh, Prediction of shear strength and behavior of RC beams strengthened with externally bonded FRP sheets using machine learning techniques, Compos. Struct. 234 (2020), https://doi.org/10.1016/j.compstruct.2019.111698 https://doi.org/.

[27] H. Naderpour, S.A. Alavi, A proposed model to estimate shear contribution of FRP in strengthened RC beams in terms of Adaptive Neuro-Fuzzy Inference System, Compos. Struct. 170 (2017) 215–227, https://doi.org/10.1016/j.compstruct.2017.03.028, https://doi.org/.

[28] T. Elgamal, M. Yabandeh, A. Aboulnaga, W. Mustafa, M. Hefeeda, sPCA: Scalable Principal Component Analysis for Big Data on Distributed Platforms, in: Proceedings of the 2015 ACM SIGMOD International Conference on Management of Data, Association for Computing Machinery, Melbourne, Victoria, Australia, 2015, pp. 79–91, https://doi.org/10.1145/2723372.2751520, https://doi.org/.

[29] F. Pourkamali-Anaraki, S. Becker, Preconditioned Data Sparsification for Big Data With Applications to PCA and K-Means, IEEE Trans. Inf. Theory 63 (5) (2017) 2954–2974, https://doi.org/10.1109/TIT.2017.2672725, https://doi.org/.

[30] M. Wan, S.-E. Li, H. Yuan, W.-H. Zhang, Cutting force modelling in machining of fiber-reinforced polymer matrix composites (PMCs): A review, Composites, Part A 117 (2019) 34–55, https://doi.org/10.1016/j.compositesa.2018.11.003, https://doi.org/.

[31] A. Cevik, Modeling strength enhancement of FRP confined concrete cylinders using soft computing, Expert Syst. Appl. 38 (5) (2011) 5662–5673, https://doi.org/10.1016/j.eswa.2010.10.069, https://doi.org/.

[32] W. Ben Chaabene, M. Flah, M.L. Nehdi, Machine learning prediction of mechanical properties of concrete: Critical review, Constr. Build. Mater. 260 (2020), https://doi.org/10.1016/j.conbuildmat.2020.119889 https://doi.org/.

[33] H.J. Yang, J.Y. Lee, W.-R. Yu, Carbon nanotube fiber assemblies with braided insulation layers for washable capacitive textile touch sensors, Funct. Compos. Struct. 2 (2020), 015007, https://doi.org/10.1088/2631-6331/ab797f https://doi.org/.

[34] P.-S. Shin, J.-H. Kim, K.L. DeVries, J.-M. Park, Evaluation of dispersion of MWCNT/cellulose composites sheet using electrical resistance 3D-mapping for strain sensing, Funct. Compos. Struct. 2 (2020), 025004, https://doi.org/10.1088/2631-6331/ab972f https://doi.org/.

[35] D.-H. Han, L.-H. Kang, Piezoelectric properties of paint sensor according to piezoelectric materials, Funct. Compos. Struct. 2 (2020), 025002, https://doi.org/10.1088/2631-6331/ab90e1 https://doi.org/.

[36] Y. Liu, S. Shang, S. Mo, P. Wang, H. Wang, Eco-friendly Strategies for the Material and Fabrication of Wearable Sensors, Int. J. Precis. Eng. Manuf.-Green Tech. (2020) 1–24, https://doi.org/10.1007/s40684-020-00285-5, https://doi.org/.

[37] A. Todoroki, Y. Samejima, Y. Hirano, R Matsuzaki, Piezoresistivity of unidirectional carbon/epoxy composites for multiaxial loading, Compos. Sci. Technol. (2009) 1841–1846, https://doi.org/10.1016/j.compscitech.2009.03.023.

[38] N. Jiang, J. Xu, S. Zhang, Event-Triggered Adaptive Neural Network Control of Manipulators with Model-Based Weights Initialization Method, Int. J. Precis. Eng. Manuf.-Green Tech. 7 (2020) 443–454, https://doi.org/10.1007/s40684-019-00095-4, https://doi.org/.

[39] A. Rafiq, N Merah, R. Boukhili, M. Al-Qadhi, Impact resistance of hybrid glass fiber reinforced epoxy/nanoclay composite, Polym. Test. 57 (2017) 1–11, https://doi.org/10.1016/j.polymertesting.2016.11.005, https://doi.org/.

[40] L. Xiaoa, G. Wang, S. Qiua, Z. Han, X. Li, D. Zhang, Exploration of energy absorption and viscoelastic behavior of CFRPs subjected to low velocity impact, Composites Part B 165 (2019) 247–254, https://doi.org/10.1016/j.compositesb.2018.11.126, https://doi.org/.

[41] S. Wang, D.D.L. Chung, J.H. Chung, Impact damage of carbon fiber polymer–matrix composites, studied by electrical resistance measurement, Composites Part A 36 (2005) 1707–1715, https://doi.org/10.1016/j.compositesa.2005.03.005.

[42] D.G. Meehan, S. Wang, D.D.L. Chung, Electrical-resistance-based Sensing of Impact Damage in Carbon Fiber Reinforced Cement-based Materials, J. Intell. Mater. Syst. Struct. 21 (2010), https://doi.org/10.1177/1045389x09354786.

[43] M Hemath, S Mavinkere Rangappa, V Kushvaha, H.N. Dhakal, S Siengchin, A comprehensive review on mechanical, electromagnetic radiation shielding, and thermal conductivity of fibers/inorganic fillers reinforced hybrid polymer composites, Polym. Compos. 41 (10) (2020) 3940–3965, https://doi.org/10.1002/pc.25703, https://doi.org/.

[44] V Kushvaha, S.A Kumar, P Madhushri, Dynamic fracture toughness index: a new integrated methodology for mode-I fracture behaviour of polymer composite under impact loading, Mater. Res. Express 6 (11) (2019), 115342, https://doi.org/10.1088/2053-1591/ab4e35 https://doi.org/.

[45] A Sharma, S.A Kumar, V Kushvaha, Effect of aspect ratio on dynamic fracture toughness of particulate polymer composite using artificial neural network, Engineering Fracture Mechanic 228 (2020), https://doi.org/10.1016/j.engfracmech.2020.106907 https://doi.org/.

[46] V Kushvaha, S.A Kumar, P Madhushri, A Sharma, Artificial neural network technique to predict dynamic fracture of particulate composite, J. Compos. Mater. 54 (22) (2020) 3099–3108, https://doi.org/10.1177/0021998320911418,

[47] A Sharma, V Kushvaha, Predictive modelling of fracture behaviour in silica-filled polymer composite subjected to impact with varying loading rates using artificial neural network, Eng. Fract. Mech. 239 (2020), 107328, https://doi.org/10.1016/j.engfracmech.2020.107328 https://doi.org/.